energies

MDPI

Article

Advanced Prototype of an Electrical Control Unit for an MR Damper Powered by Energy Harvested from Vibrations

Arkadiusz Kozieł, Łukasz Jastrzębski * and Bogdan Sapiński

Department of Process Control, Faculty of Mechanical Engineering and Robotics, AGH University of Science and Technology, Mickiewicza 30 Av., 30-059 Krakow, Poland; akoziel@agh.edu.pl (A.K.); deep@agh.edu.pl (B.S.)
* Correspondence: jastrzeb@agh.edu.pl

Abstract: The work deals with a newly developed prototype of an electrical control unit (ECU) for a magnetorheological (MR) damper powered by energy harvested from vibrations. The ECU, consisting of a rectifying bridge, a driver unit, a microcontroller, and an internal power supply system, is an advanced version of the specially designed processing system for energy harvested from vibrations and the use of this energy to control the MR damper. Unlike a typical MR damper control system in which electrical circuits are powered from an external energy source, the ECU is powered by a part of the energy extracted from a vibrating system using an electromagnetic harvester. However, the excess amount of energy recovered over that necessary to power the MR damper and electrical circuits can be collected in harvested energy storage. The study presents the design concept of the ECU, computer simulations of the in-built driver unit (DU), the method of connecting the ECU with the harvester, the MR damper and displacement sensors, and also describes experimental tests of the engineered unit applied in a vibration reduction system (VRS) with an energy recovery function.

Keywords: electrical control unit; electromagnetic harvester; MR damper; driver unit; energy storage; vibration reduction system

Citation: Kozieł, A.; Jastrzębski, Ł.; Sapiński, B. Advanced Prototype of an Electrical Control Unit for an MR Damper Powered by Energy Harvested from Vibrations. *Energies* **2022**, *15*, 4537. https://doi.org/10.3390/en15134537

Academic Editors: József Vásárhelyi, Jarosław Konieczny and William Holderbaum

Received: 24 May 2022
Accepted: 20 June 2022
Published: 21 June 2022

1. Introduction

The kinetic energy present in vibrating systems is usually converted into heat and irrevocably lost. This energy, however, can be extracted from the system and converted into electrical energy using harvesters with various transduction mechanisms (piezoelectric, electromagnetic, electrostatic) and requirements ranging from large- to small-scale power [1]. For example, piezoelectric harvesters provide a very small amount of power and are an alternative to conventional power sources (e.g., batteries) for small-sized and low-power electronic devices, like sensors. Advancement in this field was reviewed in [2] and again a decade later in [3]. One of the latest research reports on piezoelectric vibration energy-harvesting techniques is that presented in [4]. The study proposes a self-powered and low-power enhanced double synchronized switch harvesting circuit which can automatically adapt to the sinusoidal voltage signal with the wide frequency range that is released by the piezoelectric vibration energy harvester.

Widely covered in the literature are also electromagnetic harvesters which have great potential for converting mechanical energy into electrical energy. For example, the study [5] presents an electromagnetic energy harvester for human motion. The harvester managed to generate 0.3–2.46 mW of power from human body motion, and supplied body-worn sensors or electronic devices. A similar issue was considered in [6]. The authors conducted a theoretical study of an electromagnetic transducer with a conditioning circuit (full-bridge rectifier and buck–boost converter with a resistance load) which was able to generate power in the range of 1.4 mW to 90 mW. The work [7] demonstrates an electromagnetic harvester for a linear MR damper with application in a vibration reduction system that generated a maximum power of 1.8 W at 0.16 m/s vibrating speed. The harvester was an improved

version of the previously developed device reported in [8]. In the study [9], a tubular linear electromagnetic transducer was proposed for applications of large-scale vibration energy harvesting from vehicle suspensions, tall buildings, or long-span bridges. It was reported that the device was able to produce a maximum power of 2.8 W at 0.11 m/s vibrating speed. The work [10] describes fabrication and experimental verification of an electromagnetic shock absorber prototype with a cored-type tubular generator equipped with a novel combination of classical Halbach array and iron spacers for application in electric vehicles. The device was able to generate a maximum power of 225 W at 0.25 m/s vibrating speed. Advancements in energy-harvesting technology with MR dampers were made in [11]. A general review of electromagnetic energy-harvesting techniques for autonomous sensor applications was presented in [12]. It is worth mentioning that some electromagnetic harvesters of special structure can provide an amount of power large enough to power actuators, such as MR dampers.

The key limitation of vibration harvesting techniques is that the power output performance is seriously subject to the resonant frequencies of the vibrating system. To overcome this limitation, a great deal of effort has been made to develop efficient energy harvesters by adopting new materials and optimising harvester devices. Another problem is that harvesters excited by the vibrating system produce an alternating voltage or AC power, which has to be processed before it can be effectively used with any sensor or actuator requiring DC power.

In a typical architecture of a vibration energy-harvesting system, the harvester is located in the first stage of the system. It is used to convert kinetic energy of vibrations into electrical energy. The output of the harvester is an AC waveform, and therefore it has to be processed by a power converter to produce a suitable DC output voltage to meet the requirements of a sensor or an actuator requiring DC power. The power converter consists of a front-end rectifier which converts AC to DC and a standard buck or boost DC–DC converter that regulates the DC voltage. The efficiency of an energy-harvesting system depends on the power extraction and conversion efficiency of the rectifier, and the efficiency of the DC–DC converter. Therefore, a high-performance rectifier with high power extraction and conversion efficiency is essential for a high-efficiency vibration energy-harvesting system.

The simplest energy-harvesting system is a full-wave rectifier integrated with a smoothing capacitor. Such systems have been discussed in a large number of studies. For example, the study [13] reports an H-bridge Graetz rectifier with a smoothing capacitor and photorelay to convert AC voltage generated by the electromagnetic harvester to power an MR damper in a vibration control system. In the work [14], research on linear electromagnetic devices for both vibration damping and energy harvesting is described. The developed devices were able not only to dissipate the kinetic energy caused by earthquakes, wind, or traffic loads, but also to store using energy-harvesting electric circuits connected to them. Four circuit configurations of the devices were analysed: an open circuit, a circuit with a constant resistor, a circuit with a full-wave rectifier and supercapacitor, and a circuit with a full-wave rectifier and rechargeable battery. It was revealed that the damping force of the devices depends on the type of circuit connected to the output and their operation is similar to that of a viscous damper when it is connected to a resistor. Following this, the work [15] demonstrates devices which were additionally equipped with a full-wave rectifier and a buck–boost converter controlled by a low-power microcontroller. The buck–boost converter with adaptive duty cycle control could maintain a nearly constant resistance in a wide operation range and a peak output power of about 200 mW at an acceleration of 2.7 m/s^2 was achieved. The study [16] presents a self-powered vibration control and monitoring system that consisted of a pendulum-type tuned mass damper, a rotary electromagnetic device, an energy-harvesting circuit (full-wave bridge, DC–DC converter, Li-ion battery), and a wireless smart sensor. The experimental results revealed that the harvested power reached about 312.4 mW with random ground motions with root-mean-square acceleration equal to 0.05 g. Also, the work [17] shows experimental investigation into an

application of an electromagnetic device on bridge stay cables for simultaneous energy harvesting and vibration damping. A device equipped with a full-wave bridge rectifier and buck–boost converter used to charge a battery was attached to a 5.85 m long scaled stay-cable model and was able to generate 44.1 mW of output power in resonant vibration. The authors of the work [18] designed a vibration energy harvester compound of a dual-mass damper system with a linear electromagnetic transducer, a full-wave bridge, and a storage capacitor and clarified system effectiveness concerning energy harvesting from bridge vibrations. The study [19] reports an H-bridge Graetz rectifier with a smoothing capacitor to convert AC current generated in a resonant electromagnetic vibration harvester into DC current supplying resistance load. The work [20] demonstrates a measurement and control unit with an H-bridge Graetz rectifier for conditioning the energy recovered from an object's oscillations in an MR rotary damper-based positioning system.

The task of the ECU demonstrated in this study is to adequately adjust the voltage generated by an electromagnetic harvester for powering a commercial MR damper in a VRS. It should be noted that the present work does not concern the optimization of the harvester. Assumptions for the ECU project were determined on the basis of tests carried out for an H-bridge Graetz rectifier developed by the authors with N-type MOSFETs [21] and the results of experimental tests of a VRS [22]. The results of these studies showed that at kinematic excitation frequencies of the system greater than $\sqrt{2}$ times its resonance frequency, the amplitude of vibrations of a sprung mass increases, which is an undesirable phenomenon. To prevent this, the current in the MR damper control coil must be shaped appropriately over the entire excitation frequency range. If this coil is powered by the output voltage of the harvester, this can be achieved either by using a capacitor bank with an appropriate capacity and cutting off the MR damper from the power source at higher frequencies [23], or by connecting/disconnecting the harvester coil and the MR damper control coil in accordance with the adopted algorithm. In this paper, the authors showed that this problem can be solved by introducing the developed ECU into the VRS. When designing the ECU, particular emphasis was placed on reducing energy losses resulting from powering its components as much as possible.

The study is structured as follows: Section 2 describes the design concept of the ECU prototype. Section 3 benchmarks simulation results of the driver unit embedded in the ECU with special emphasis of current consumption and efficiency analysis. Section 4 reveals the structure of the engineered ECU and presents experimental results of the unit applied in the VRS. Final conclusions are drawn in Section 5.

2. Design Concept and Operating Principle of the Electrical Control Unit

The operation of the ECU is to connect/disconnect the MR damper control coil (electrical load) to/from the harvester coil (source of electrical energy recovered from vibrations). The architecture of the ECU is shown in Figure 1. The unit consists of a bridge rectifier (RB), driver unit (DU), microcontroller (μC), and internal power supplier (IPS). The operation of the ECU is controlled by a 32-bit microcontroller with an ARM Cortex M4 core, which produces a control signal according to the implemented control algorithm and performs measurement functions. All electronic components of the ECU do not require external power supply. The authors engineered two versions of the ECU differing in the design and operation of the embedded DU when μC does not generate a control signal. In such cases, the MR damper control coil is disconnected by default (N.O. version) or connected (N.C. version) to the power source. Due to the fact that both versions differ in the default polarity of their power transistor gates, in Sections 2 and 3 we present a design concept and simulation tests only for the ECU in its N.C. version. However, the differences in the operation of the unit in N.C. and N.O. versions were experimentally tested by introducing the ECU into a VRS and this issue is discussed in Section 4.

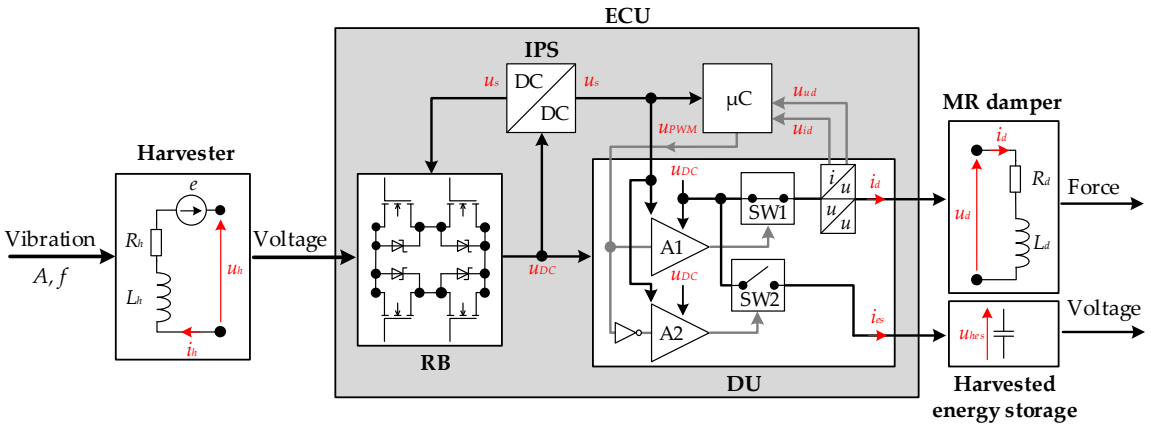

Figure 1. Architecture of the electrical control unit.

The μC block controlling the work of the ECU was implemented on a commercial NUCLEO-L031K6 evaluation set [24] with an STM32L031K6T6 microcontroller equipped with an internal linear voltage regulator and circuits allowing programming and debugging of the microcontroller. The purpose of the RB block is to convert the AC voltage generated by the harvester into DC voltage. Due to the replacement of Schottky diodes with MOSFET transistors with dedicated control circuits, the efficiency of energy conversion is over 90%. This reduces the loss of energy transferred from the harvester to the MR damper. The DU unit acts as an electric power flow-control system. It enables connecting/disconnecting the MR damper control coil to/from the RB block depending on the logic state of the u_{PWM} signal generated by the μC block. An additional function of the DU block is the possibility of optionally attaching harvested energy storage to it. As a result, when the MR damper control coil is disconnected, it is possible to store electricity. In addition, in the DU block there are built-in circuits enabling the measurement of voltage and current in the MR damper control coil. The IPS block generates a stabilized 3.3 V voltage output, which supplies the following units: RB, DU, and μC. The applied DC–DC converter type TPS61200 [25] based on the BOOST topology exhibits stable operation when its input voltage u_{DC} > 0.3 V and provides a current of about 1 A taken from its output. The assumptions adopted in the ECU project take into account the electrical parameters of the harvester, RB, MR damper, VRS dynamic properties (in which the ECU was tested), and the parameters of kinematic excitation (vibration with amplitude A and frequency f) that set the system in motion.

Figure 1 presents the architecture of the ECU and also the method of connecting this unit to the harvester coil and the MR damper control coil and the optional harvested energy storage. The AC voltage u_h generated by the harvester is converted to DC voltage u_{DC} in the RB block. The DU block decides whether the voltage u_{DC} will supply the MR damper control coil or harvested energy storage. The choice of the energy receiver (MR damper control coil or harvested energy storage) depends on the logic state of the voltage u_{PWM} generated by μC. The voltage u_{PWM} has a frequency of 1 kHz and a modified pulse width. Rapid switching between the MR damper control coil and harvested energy storage is performed by two SW1 and SW2 keys built on MOSFET type transistors, which are characterized by low power loss. The gate control of these transistors requires u_{PWM} voltage amplification. This gain is realized by the gain paths A1 and A2. In order for only one SW1 or SW2 key to remain on, it is necessary to negate the voltage u_{PWM} before connecting it to the A2 input. Voltage u_d and current i_d in the MR damper control coil are measured by the transducers i/u and u/u built on the measurement amplifiers. The transducers i/u and u/u convert the voltage u_d and the current i_d into voltages u_{ud} and u_{id} in the range (0, 3.3) V, which are fed to the input of the A/D converter built into the μC. The gain path A1, A2, and transducers i/u and u/u are supplied by IPS output voltage u_s, while keys SW1 and SW2 are supplied directly with u_{DC} voltage.

The correct control of the output voltage from the ECU that powers the MR damper control coil depends primarily on the DU switching on/off the control coil quickly. This requires accurate measurement of the current in the MR damper control coil in order to implement the two-state current controller in the µC. Considering the above, the following assumptions were made for the design of the DU:

- The DU operates as a voltage amplifier u_{PWM}: with a constant switching frequency of 1 kHz, variable duty cycle (0, 100)%, and a minimum voltage of 1.6 V;
- The SW1 key, which control the current i_d, works as a normally closed key and in the absence of voltages u_{PWM} or u_s connects u_{DC} voltage continuously to the MR damper control coil. The SW2 key charging the energy storage works as a normally open key;
- The DU is designed to operate at a maximum voltage of u_{DC} not exceeding 10 V;
- The internal amplifier circuits require a constant voltage u_s = 3.3 V produced by IPS (DC–DC BOOST converter).
- The DU provides separation of the control voltage of the u_{PWM} from the output voltages of u_d and u_{hes};

It should be noted that the DU can be adapted to operate at higher frequencies of voltage u_{PWM}, as well as higher supply voltage u_{DC} than those outlined in the assumptions. Figure 2 shows the architecture of the DU. There are three groups of electrical circuits designated as S1, S2, and S3.

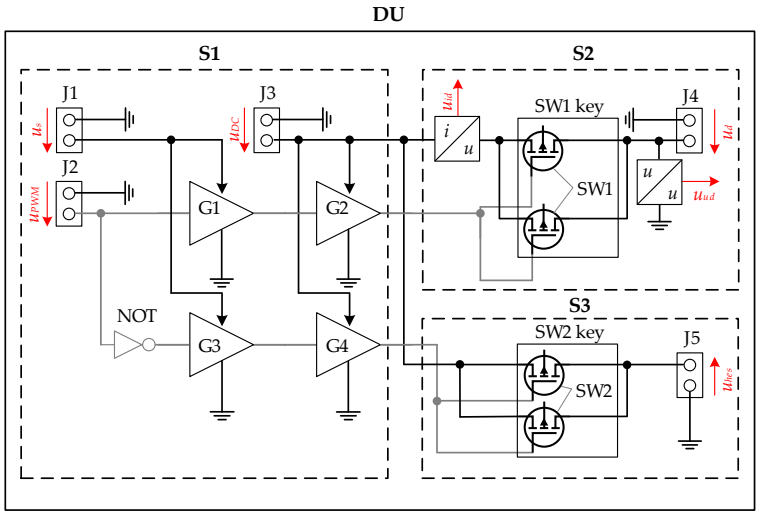

Figure 2. Architecture of the driver unit.

In the S1 group, there are four amplifiers G1–G4 made of two types of complementary bipolar transistors (NPN/PNP). G1 and G3 amplifiers, powered by voltage u_s = 3.3 V (J1 connector), are used to isolate the voltage u_{PWM} (J2 connector) from the voltage u_{DC} (J3 connector). In the absence of voltage u_{PWM} (high-impedance state), the potentials on the bases of the transistors of the amplifiers G1 and G3 correspond to the potentials of their emitters, which results in the lack of current in the bases of these transistors and their cut-off mode. This allows the SW1 and SW2 keys to be in the default states (not forced by the control). In the N.C. version, the default states are the saturation state of the SW1 transistor and cut-off state of the SW2 transistor. However, in the N.O. version, the default states of the transistors are opposite. At the input of the G3 amplifier, a transistor circuit is used to realize a NOT logical function in order to negate the voltage u_{PWM}. Negation allows SW1 and SW2 transistor keys to work in a counter phase. G2 and G4 amplifiers act as preamplifiers for the SW1 and SW2 transistor keys. Thanks to this, the voltages and currents at the output of the G2 and G4 amplifiers are appropriately adjusted to work with the SW1 and SW2 keys. The task of G2 and G4 amplifiers is to charge and discharge the capacities of the gates of the transistors from which the SW1 and SW2 keys are built.

The group S2 shows details of the SW1 key circuit with transducers i/u and u/u. The SW1 key contains two P-channel MOSFETs transistors connected in parallel. The selected transistors are characterized by a gate-source breakdown voltage $u_{GS} \leq -0.4$ V. This allows the DU to operate when the voltage $u_{DC} \geq 0.4$ V. The drain current of a single-transistor SW1 is only 0.47 A. Therefore, it is recommended to use at least two transistors connected in parallel. Since in most cases the voltage u_{DC} does not exceed 3 V, two transistors provide a drain current of 1 A assuming that $u_{GS} = -3$ V. To measure the current i_d, a differential amplifier INA181A4 [25] was used, which measures the voltage at the 10 mΩ shunt resistor. The differential gain of the measuring amplifier is 200 V/V. A resistive divider with a voltage divider ratio of 0.32, connected in parallel to the MR damper control coil (connector J4), was used to measure the voltage.

In the group S3 there is a SW2 key made of the same transistors as the SW1 key. Since the task of the SW2 is to transfer energy from the harvester to the energy storage ($u_{hes} = u_{DC}$) when the MR damper control coil is not powered, no measuring circuits are used here. It should be noted that the voltage and current charging the energy storage are not measured, because these values are not used by the control algorithm.

3. Simulation Tests of the Driver Unit

Computer simulations were aimed at checking the correctness of switching the SW1 and SW2 keys and determining the current consumption and DU efficiency. The simulations were carried out in the LTspice environment [26]. It was assumed that the power consumption and efficiency of the RB would not be analyzed, as this issue was described in detail in [21]. In addition, the current consumption by measuring circuits (resistive dividers and measuring amplifiers) and the scattering of parameters of electronic components resulting from the tolerance of their performance were not taken into account. The following assumptions were adopted for the simulation:

- The transistor keys SW1 and SW2 are created of two MOSFETs connected in parallel to channel P-type BSH203 [27];
- The G1–G4 amplifiers are created of complementary bipolar transistors BC849 (NPN) and BC859 (PNP) [27];
- The voltage u_s supplying measurement systems and amplifiers G1 and G3 were assumed to be in the range (1.6, 3.6)V, the typical voltage is u_s = 3.3 V;
- The voltage u_{DC} supplying the amplifiers G2 and G4 and the keys SW1 and SW2 were adopted in the range of (0, 10)V;
- In the absence of voltage u_{PWM} (high-impedance state), the DU sets the keys SW1 and SW2 to the default state;
- The MR damper control coil is represented by the one-port circuit R_dL_d (L_d = 100 mH, R_d = 5 Ω);
- Harvested energy storage is represented by the resistor R_{hes} = 4.7 Ω.

Two modes of DU operation were defined, nominal and standby, assuming supply voltages of u_s = 3.3 V and u_{DC} = 3 V. In the nominal mode, a PWM signal with a frequency of 1 kHz and a duty cycle of 50% was generated. In standby mode, the µC output on which the control voltage u_{PWM} is generated assumes a high-impedance state. The SW1 and SW2 keys have default states. Simulated current consumptions i_s and i_{DC} and power consumptions P_s and P_{DC} from the voltage sources u_s and u_{DC}, respectively. Total power P_t consumed by the DU is the sum of powers P_s and P_{DC}. The results of the simulation of current consumption by the DU were verified in measurements made using a Fluke 8845 A multimeter [28]. The measurements were carried out at voltage u_{DC} 0.7, 1.2, and 4 V. These values of voltage u_{DC} correspond to the values obtained in the ECU tests installed in the VRS at f equal to 3.3 Hz (IPS stable operation), 3.8 Hz (resonance frequency), and maximum excitation frequency 10 Hz (see Section 4), respectively. Table 1 shows the measurement points M1–M8 (see Figures 3 and 4) and the conditions at which the current consumption was measured.

Table 1. Conditions of current-consumption measurements.

Marker	DU mode	Condition
M1	Standby	u_s = 3.3 V
M2	Nominal	u_s = 3.3 V
M3	Standby	u_{DC} = 0.7 V
M4	Standby	u_{DC} = 1.2 V
M5	Standby	u_{DC} = 4 V
M6	Nominal	u_{DC} = 0.7 V
M7	Nominal	u_{DC} = 1.2 V
M8	Nominal	u_{DC} = 4 V
M9	Standby	u_{DC} = 0.7 V
M10	Standby	u_{DC} = 1.2 V
M11	Standby	u_{DC} = 4 V

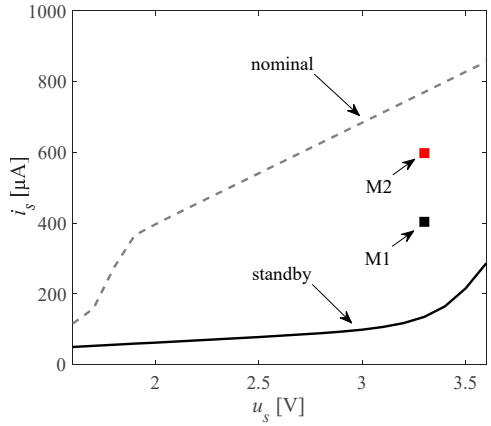

Figure 3. Current i_s vs. voltage u_s.

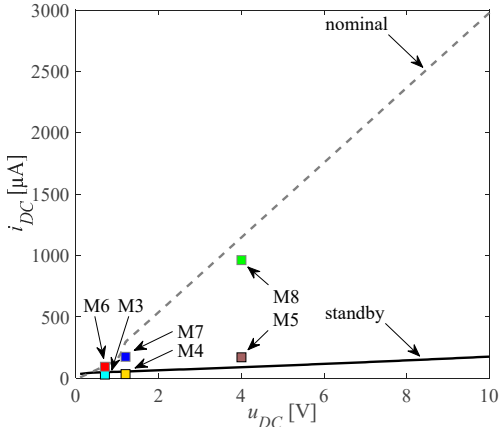

Figure 4. Current i_{DC} vs. voltage u_{DC}.

The simulation results are shown in Figures 3–7. The graphs of Figure 3 show current consumption i_s vs. u_s, and the graphs of Figure 4 show current consumption i_{DC} vs. u_{DC}. Analysing the graphs in Figures 3 and 4, it can be seen that in the nominal operating mode, the DU draws a current more than 2.5 times greater, both from the source u_s and u_{DC} compared to the standby mode. The maximum values of current i_s and i_{DC} in nominal mode are 850 µA and 3 mA, respectively, and in standby mode 300 µA and 150 µA. The power consumption of i_s and i_{DC} in the standby mode results mainly from the polarity of the bases of the transistors from which the G1–G4 amplifiers are built. In nominal mode, the increased current consumption is the result of periodic charging and discharging of the gates of the keying transistors SW1 and SW2. When comparing the results obtained from

the simulation and the measurements at points M1 and M2, a significant difference can be observed (see Figure 3). The measured current consumption of DU in standby mode (point M1) is about 400 µA and is higher by about 275 µA compared to the result obtained from the simulation. This difference is most likely due to the fact that the current consumed by the INA181 measuring amplifier was not included in the simulation. The typical value of the current consumed by this amplifier is 195 µA. The measured current consumption by DU in nominal mode (point M2) is smaller than that obtained from the simulation. In this case, the difference may result from the tolerance of the electronic components used to build the DU. Measuring points M3–M8 (Figure 4) confirm the compliance of simulation data with measurement results.

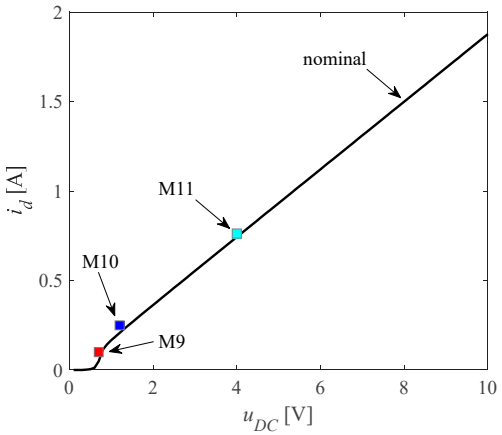

Figure 5. Current i_d vs. voltage u_{DC}.

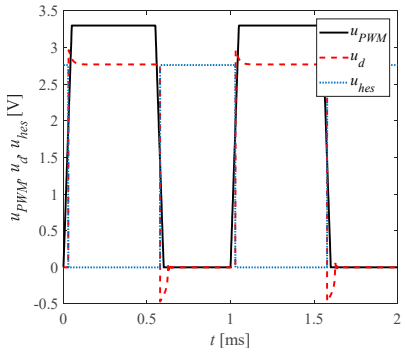

(**a**)

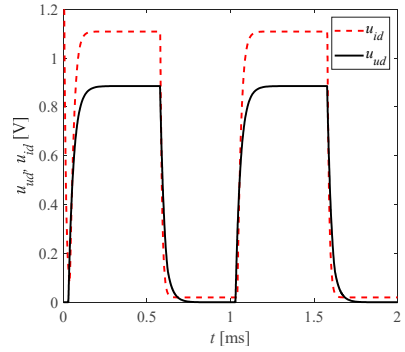

(**b**)

Figure 6. Time histories of voltages: (**a**) u_{PWM}, u_d, u_{hes}; (**b**) u_{id}, u_{ud}.

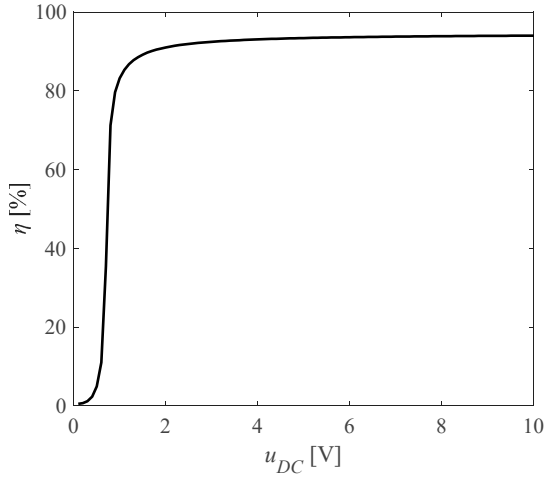

Figure 7. Efficiency η vs. voltage u_{DC}.

In subsequent simulations, the relationships between the current i_d and the voltage u_{DC} were determined. The results of these simulations are shown in Figure 5. The determined relationship of i_d vs. u_{DC} allowed us to determine the minimum voltage u_{DC}, at which SW1/SW2 keys operate with the greatest efficiency. As can be seen with voltage u_{DC} higher than 0.8 V, the SW1/SW2 key transistors are fully opened (saturation mode). Above this voltage value, the relationship i_d vs. u_{DC} becomes linear. This means that the resistance of the transistor channel is constant. The slope of the graph i_d vs. u_{DC} results from the resistance R_d of the control coil. The graphs of Figure 5 show the compliance of simulation results with measurement data (see markers M9–M11). Figure 6a presents the time waveforms of voltages u_{PWM}, u_d and u_{hes}, and Figure 6b shows the time waveforms u_{id} and u_{ud} in the DU operating in nominal mode. It should be noted that the voltage u_d is compatible in phase with the voltage u_{PWM}, but shifted in phase with respect to the voltage u_{hes} by 180°, which means that the recovered energy is always transferred at the same time either to the MR damper control coil or to the harvested energy storage. The graphs of Figure 6b show the voltages u_{id} and u_{ud} at the output of the transducers i/u and u/u.

Figure 7 presents the dependence of efficiency η on voltage u_{DC} of the DU. The graph shows that the DU starts to operate above 0.4 V. When the voltage u_{DC} reaches values between 0.4 V and 2 V, the DU has limited efficiency. When the voltage u_{DC} is higher than 2 V, the efficiency reaches the maximum value of approx. 94%. This efficiency can be increased by selecting power transistors with less open-channel resistance or by multiplying the number of parallel-connected transistors that make up the SW1 key. In the developed DU, its efficiency was increased by multiplying the number of transistors. Table 2 summarizes the power consumptions P_s, P_{DC}, and P_t from the DU operating in nominal and standby mode. As can be seen, the maximum power demand P_t does not exceed 6 mW.

Table 2. Power consumption of the driver unit.

DU Mode	u_s [V]	u_{DC} [V]	P_s [mW]	P_{DC} [mW]	P_t [mW]
nominal	3.3	0.7	1.98	0.065	2.045
	3.3	1.2	1.98	0.2	2.180
	3.3	4	1.98	3.848	5.828
standby	3.3	0.7	1.32	0.0196	1.3396
	3.3	1.2	1.32	0.0384	1.3584
	3.3	4	1.32	0.68	2

4. Experimental Testing of the Electrical Control Unit in the Vibration Reduction System

Experiments of the ECU were carried out in the experimental setup (see diagram in Figure 8). The experimental setup included an electromagnetic harvester [7], an MR damper of the RD 8040-1 series [29], a spring with stiffness k = 90,000 N/m, and sprung mass m = 155 kg. The resonance frequency of the VRS is f_r = 3.8 Hz. The ECU was located between the harvester coil and the MR control coil in the VRS (spring-MR damper-sprung mass) damper control coil. The measuring system of the experimental setup consisted of a PC, an AD/DA board, laser displacement sensors, strain gauges force sensors, voltage–voltage transducers (u/u), and current–voltage transducers (i/u). This system allows for the measurement of the following quantities: displacement of the shaker core z (excitation), sprung mass displacement x, input force F_{in}, MR damper force F_d, harvester coil voltage and current u_h and i_h, and control coil voltage and current MR damper u_{DC} and i_{DC}.

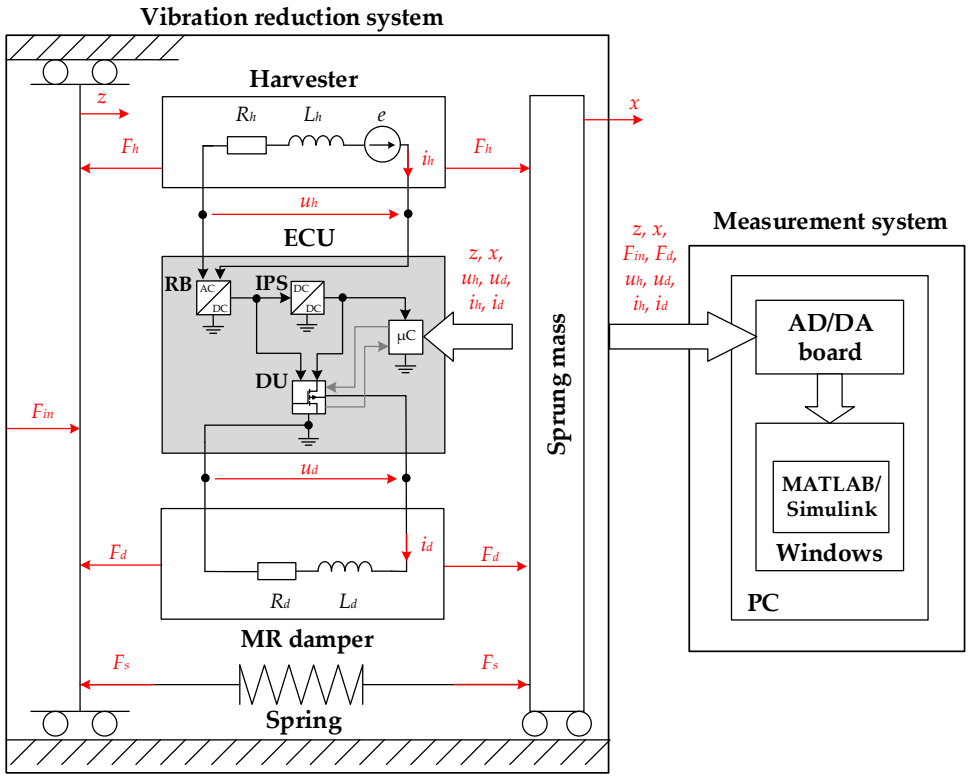

Figure 8. Schematic diagram of the experimental setup.

At the present stage of the research, harvested energy storage was not used, therefore it was not connected to the ECU. Correct control of switching on/off the MR damper control coil to/from the harvester coil required vibration measurements in the VRS. Displacements in the system were measured using EN1 and EN2 SME53 linear magnetic encoders [30] connected to the ECU. The choice of these encoders was determined by the ease of connection to µC (push–pull output) and low demand for computing power when processing the generated pulses to the speed required by the algorithm (embedded 16-bit timers). The EN1 and EN2 encoders were the only elements of the VRS that were powered from an external 24 V (EPS) voltage source. The need for such power supply of the EN1 and EN2 encoders resulted from the large current consumption during switching on (DC–DC converters are built into the encoders), which meant that the momentary amount of energy needed to supply them was greater than that recovered from vibrations.

Electrical connections of the ECU to the harvester coil, the MR damper control coil, and the encoders EN1 and EN2 are shown schematically in Figure 9, along with a photograph of the PCB circuits (RB, IPS, µC, and DU) in Figure 10. Lines in black indicate the energy flow

in the system, while lines in grey indicate the control and measurement signals. It should be noted that for the measurement of displacements z and x, two types of sensors were used independently: laser for data acquisition (not visible in Figure 8), and the encoders EN1 and EN2 to develop a control signal by the ECU (Figure 9).

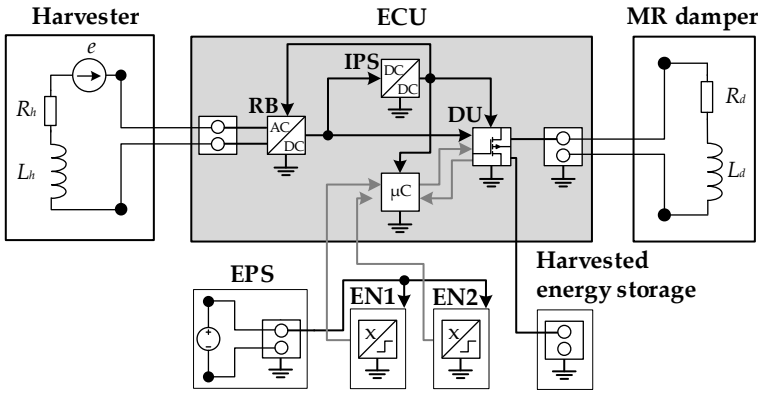

Figure 9. Connections in the harvester–electrical control unit–MR damper system.

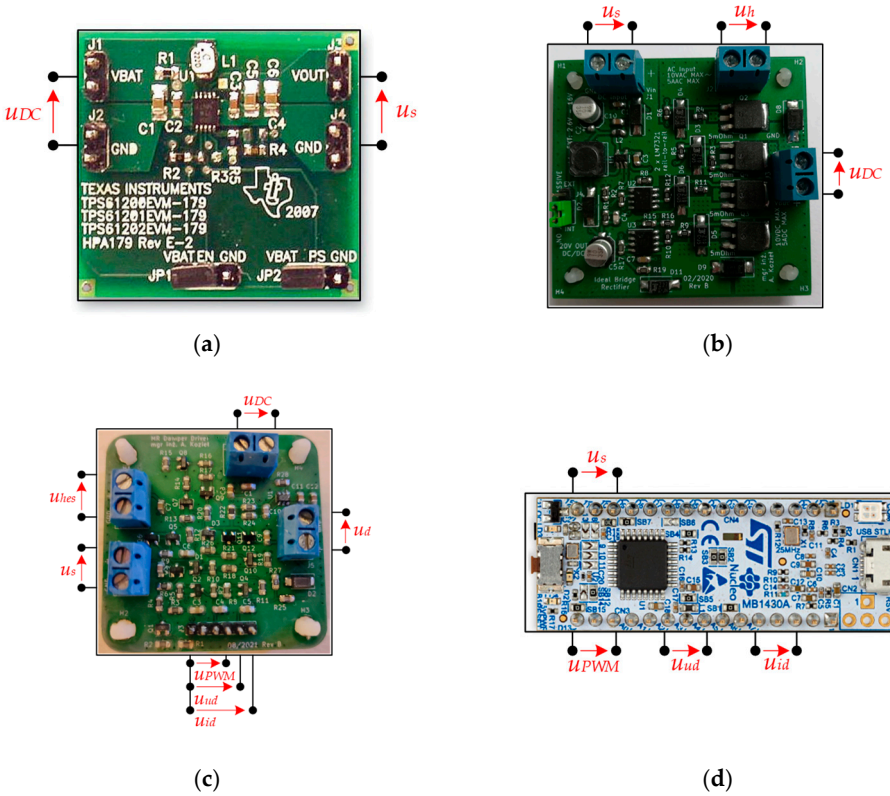

Figure 10. Components of the electrical control unit: (**a**) IPS [25]; (**b**) RB [21]; (**c**) DU; (**d**) µC [24].

There are various control strategies for application systems utilizing smart devices based on MR fluids [31]. The use of an appropriate control algorithm is a critical factor because it is the final action stage of the application to obtain the desired output response. For the purpose of the research described in this work, the authors implemented the sky-hook control scheme [32] in the µC. It should be noted that the current in the MR damper control coil only affects the amount of dissipated energy (it is not possible to perform mechanical work). This results in the need to use a modified sky-hook algorithm for semi-active systems, in which the setpoint current i_{set} is calculated in accordance with Equation (1). In order for the measured value of current i_d to correspond to the value of i_{set} calculated

according to the algorithm, a on–off current controller was used to determine the voltage u_{PWM} according to the Equation (2). The ratio k = 2 A·s/m was selected experimentally.

$$i_{set} = \begin{cases} k|\dot{x}| \; ; \; \dot{x}(\dot{x} - \dot{z}) > 0 \\ 0 \; ; \; \dot{x}(\dot{x} - \dot{z}) \leq 0 \end{cases} \tag{1}$$

$$u_{PWM} = \begin{cases} 3.3 \text{ V} \; ; \; i_d < i_{set} \\ 0 \text{ V} \; ; \; i_d \geq i_{set} \end{cases} \tag{2}$$

The experiments were carried out with excitation z with an amplitude A = 3.5 mm and frequency f changed from 2 Hz to 10 Hz with a 0.1 Hz step. In each experiment lasting 20 s, three time intervals were distinguished: increasing the amplitude (0, 5) s, maintaining a constant amplitude (5, 15) s, and reducing the amplitude (15, 20) s. The results of experiments performed at a constant amplitude of excitation z are shown in Figures 11 and 12. The plots in Figure 11 show the powers generated by the harvester P_h, supplied to the MR damper control coil P_d, and consumed by the ECU P_{el} vs. frequency f. The power values P_h, P_d, and P_{el} were calculated according to the Equations (3)–(5).

$$P_h = P_d + P_{el} \tag{3}$$

$$P_h = P_d + P_{el}; P_h = \frac{1}{N} \sum_{j=1}^{N} u_{hj} i_{hj} \tag{4}$$

$$P_d = \frac{1}{N} \sum_{j=1}^{N} u_{DCj} i_{DCj} \tag{5}$$

where N is the total number of u_{DC} and i_{DC}-registered samples.

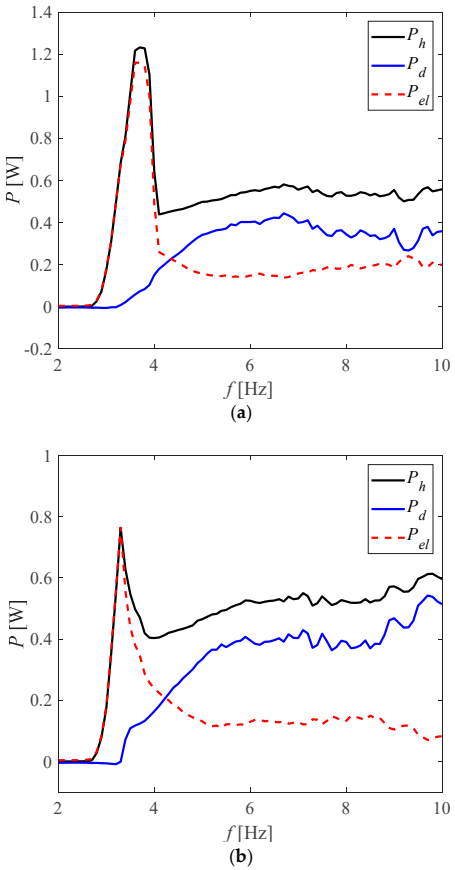

Figure 11. Powers P_h, P_d, P_{el} vs. frequency f: (**a**) ECU N.O. version; (**b**) ECU N.C. version.

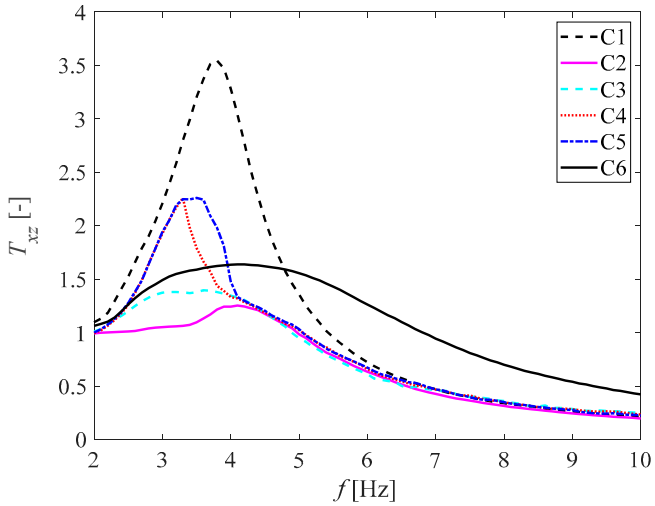

Figure 12. Transmissibility coefficient T_{xz} vs. frequency f.

In Figure 11, three characteristic frequency ranges f can be distinguished: (2, 3) Hz, (3, 4) Hz, and (4, 10) Hz. Zero power values P_h, P_d, and P_{el} in the range (2, 3) Hz result from the relative speed $(\dot{x} - \dot{z})$ insufficient to generate voltage u_h. In the range (3, 4) Hz, the harvester voltage u_h increases, which also increases the voltage u_{DC} at the output of the RB block. The DC–DC converter in the IPS block attempts to start when $u_{DC} > 0.3$ V. During the startup of the converter, the highest current consumption by the ECU circuits occurs, related to charging the internal capacitors of the converter ($P_{el} = P_h$). The peak power P_h is about 1.2 W for the ECU N.O. version (Figure 11a) and 0.75 W for the ECU N.C. version (Figure 11b). The reason for the difference in peak power values P_h are the different relative speed values $(\dot{x} - \dot{z})$ in the VRS. In the N.C. version, due to the default connection of the MR damper control coil with the output of the RB block, the current i_d appears when $u_{DC} > 0$ V. In the ECU N.C. version, at the same excitation f frequency, the damping in the VRS is higher compared to the ECU N.O. version. This results in a decrease in the relative speed $(\dot{x} - \dot{z})$, on which the voltage value u_h depends, and thus a lower peak power value P_h at the start of the IPS converter. It should be noted that in this frequency range µC is frequently restarted, which results in unstable ECU operation resulting from the lack of stable (unchanged in time) voltage generated by the IPS block. This also affects the voltage u_{PWM}, which at the moment of power loss in the µC, is not generated in accordance with the implemented algorithm. In the range (4, 10) Hz, the ECU operates stably (there is no µC reset resulting from the supply voltage). The supply voltage of the IPS unit reaches the nominal value, and the bridge RB rectifies the voltage u_h with high efficiency. As can be seen, the power P_{el} consumed by the ECU N.O. version is about 200 mW, while in the ECU N.C. version it is about 100 mW. The lower power consumption of the ECU N.C. version is associated with the shorter time required to activate the SW1-key control amplifiers.

Table 3 presents the status of RB, IPS, µC, and DU blocks included in the ECU and maximum values P_h^{max}, P_d^{max}, *and* P_{el}^{max} of powers P_h, P_d, and P_{el} in the frequency ranges of f equal to (2, 3) Hz, (3, 4) Hz, and (4, 10) Hz. As can be seen, in the range of (4, 10) Hz, all ECU blocks worked stably, and the transfer of energy from the harvester coil to the MR damper control coil took place with high efficiency. The reason for the unstable operation of the ECU in the range (3, 4) Hz was the toggling of the voltage u_s. This affected the low efficiency of the RB and DU blocks and the unstable operation of the µC and, consequently, the increase in the amplitude of the sprung mass. As can also be seen in the range (2, 3) Hz, the voltage u_h generated by the harvester was too small for the ECU to supply the MR damper control coil.

Table 3. Status of ECU blocks and maximum values of powers P_h, P_d, P_{el}.

Frequency Range	ECU Version	RB Status	IPS Status	µC Status	DU Status	u_{DC} [V]	u_S [V]	P_h^{max} [W]	P_d^{max} [W]	P_{el}^{max} [W]
(2, 3) Hz	N.O. N.C.	no rectification	no supply	no control	open circuit short circuit	<0.3	0	0	0	0
(3, 4) Hz	N.O. N.C.	low-efficiency rectification	unstable operation	unstable control	uncontrolled toggling	(0.3, 0.7)	toggling	1.2 0.75	0.1 0.15	1.1 0.75
(4, 10) Hz	N.O. N.C.	high-efficiency rectification	stable operation	stable control	stable control	>0.7	3.3	0.6 0.6	0.4 0.5	0.2 0.1

In order to evaluate the dynamic behaviour of the VRS under kinematic excitation z, we introduce displacement transmissibility $T_{xz}(f)$ which is the ratio between the amplitude of sprung mass and shaker core displacements expressed as follows:

$$T_{xz}(f) = \frac{\sqrt{\int_0^{\frac{1}{f}} x(t)^2 dt}}{\sqrt{\int_0^{\frac{1}{f}} z(t)^2 dt}} \tag{6}$$

The $T_{xz}(f)$ coefficient entered in this way was used to compare the operation of VRS in the following cases:

- Case C1: no power supply for the MR damper;
- Case C2: MR damper and ECU powered from an external source only;
- Case C3: MR damper powered by recovered energy and ECU circuits powered from an external source;
- Case C4: MR damper and ECU in N.C. version powered by recovered energy;
- Case C5: MR damper and ECU in N.O. version powered by recovered energy;
- Case C6: MR damper powered directly from the harvester.

Figure 12 shows plots $T_{xz}(f)$ for cases C1–C6. In case C1, the maximum vibration amplitude of the sprung mass occurs at the resonant frequency f_r = 3.8 Hz (T_{xz} = 3.5). When the harvester coil is directly connected to the MR damper control coil as in case C6, a significant reduction in $T_{xz}(f)$ is obtained compared to case C1 at frequencies lower than 4.8 Hz. The increase in the amplitude of vibrations of the sprung mass at frequencies higher than 4.8 Hz is an unfavourable phenomenon. This can be eliminated by turning on the ECU between the harvester coil and the MR damper control coil and controlling the current i_d. In each of the cases C2–C5, the ECU executes the same sky-hook control algorithm (formula 1, 2) to reduce the amplitude of the sprung mass over the entire frequency range f compared to case C1. The lowest vibration amplitude of the sprung mass occurs in case C2. This is because the ECU and the MR damper are powered from an external power source of unlimited power. The above confirms the correct operation of ECU electronic circuits and the correctness of the implemented control algorithm. Case C2 can therefore be treated as a reference case, for which the $T_{xz}(f)$ values will be compared with the $T_{xz}(f)$ values in cases C3–C5. As can be seen in case C2, the maximum value of this coefficient is 1.25. In case C3, the ECU's electronic circuits are still powered from an external power source (bypassing the IPS block). The MR damper control coil, on the other hand, is powered by the voltage generated by the harvester and rectified by the RB block via the DU. In case C3, in the frequency range (2, 4) Hz, it can be seen that the values of T_{xz} are higher than in case C2. This is due to the low harvester output voltage resulting from the low relative speed ($\dot{x} - \dot{z}$) and therefore the lower current level i_d in the MR damper control coil. In this case, the maximum value T_{xz} = 1.4 occurs at frequency f = 3.6 Hz. In cases C4 and C5, in which both the ECU and MR damper control coil are powered from the harvester, the vales of T_{xz} in the range (2, 4) Hz are higher than in case C3. This is due to insufficient harvester output voltage in the range (2, 3) Hz and unstable ECU operation in the range (3, 4) Hz. In cases C4 and C5, the maximum values of the T_{xz} coefficients are 2.3 and occur at frequencies of 3.2 and 3.5 Hz, respectively. Moreover, at frequencies (3.3, 4.1) Hz in case C4, the value T_{xz} is higher than in case C5. In cases C2–C5, in which the ECU is employed in the VRS,

the values of T_{xz} take similar values at frequencies higher than 4 Hz. These T_{xz} values are about 5% higher at frequencies higher than 7 Hz when compared to case C1.

Following the studies [33] and [34], we additionally introduce the frequency domain integral performance index $J_{fa,fb}$ in the frequency range (f_a, f_b), given by Equation (7), aiming at improving the efficiency of vibration damping in the VRS. The index allows us to compare the efficiency of vibration damping in the frequency range (f_a, f_b).

$$J_{f_a,f_b} = \frac{1}{f_b - f_a} \int_{f_a}^{f_b} T_{xz}(f) df \tag{7}$$

Table 4 summarizes the resonant frequency f_r, transmissibility $T_{xz}(f)$, and performance index $J_{fa,fb}$ of the VRS in cases C1–C6.

Table 4. Resonant frequency f_r, transmissibility T_{xz} (f), and performance index $J_{fa,fb}$ in cases C1–C6.

Case	f_r	T_{xz} ($f = f_r$)	T_{xz} (f = 10 Hz)	$J_{2,10}$	$J_{2,3}$	$J_{3,4}$	$J_{4,7}$	$J_{7,10}$
C1	3.8 Hz	3.50	0.22	1.6	1.56	3.06	1.24	0.31
C2	4.1 Hz	1.25	0.20	0.69	1.02	1.13	0.83	0.29
C3	3.6 Hz	1.40	0.25	0.76	1.20	1.38	0.82	0.33
C4	3.2 Hz	2.30	0.24	0.84	1.34	1.80	0.86	0.33
C5	3.5 Hz	2.30	0.23	0.88	1.35	2.09	0.87	0.32
C6	4.1 Hz	1.70	0.43	1.11	1.27	1.59	1.38	0.64

Taking into account the results in Figure 12 and in Table 4, it can be stated that the ECU introduced into the VRS and powered by the energy harvested from vibrations allows us to reduce vibration amplitude of the sprung mass in the frequency range (2, 10) Hz. It is worth mentioning that at frequencies higher than 4 Hz, the performance of the VRS in cases C4 and C5 (ECU and MR damper are powered by the harvested energy) is similar to that in case C2 (ECU is powered from an external power source). It is clearly seen that at frequencies lower that 4 Hz, the ECU needs some improvements due to the toggling effect occurring in the IPS causing unstable operation of the ECU.

5. Summary

The paper presents a newly developed prototype of the ECU for an MR damper. The advantage of the ECU is that it is powered by energy harvested from vibrations. In a situation where the MR damper does not require a power supply, harvested energy can be stored in the harvested energy storage.

The ECU was developed in two versions, an N.O. version and an N.C. version. They differ in the structure of the internal DU, the essence of which consists in the default disconnection or connection of the harvester coil from/to the MR damper control coil by the transistor in the absence of a control signal (ECU is not powered). Both versions of the ECU were subjected to experimental tests in the VRS. Based on the obtained experimental data, the power consumption and dynamic behaviour of the VRS were analyzed, taking into account displacement transmissibility $T_{xz}(f)$ and integral performance index $J_{fa,fb}$. It was found that with a stable operation of the ECU, it exhibits electrical efficiency over 90% and power consumption less than 200 mW. The results of the study lead us to the following conclusions:

- The power consumption of the ECU in the N.C. version with stable operation is approx. 100 mW, and in the N.O. version approx. 200 mW;
- In the entire tested frequency range (2, 10) Hz, the VRS with ECU shows higher efficiency of vibration damping (compare index $J_{2,10}$ in cases C2–C5 with that in case C1 and C6);

- At frequencies higher that 4 Hz, the efficiency of VRS vibration damping with an ECU powered by harvested energy is similar to the ECU powered from an external source, (compare indexes $J_{4,7}$ and $J_{7,10}$ in case C4 and C5 with that in case C2);
- At frequencies lower than 4 Hz, the unstable work of the ECU powered by the harvested energy causes an increase in the vibration amplitude of the sprung mass when compared to the ECU powered from an external source (compare indexes $J_{2,3}$ and $J_{3,4}$ in case C4 and C5 with case C2 and C3);
- In the frequency range (3.3, 4.1) Hz, the ECU in the N.C. version provides a reduction in the amplitude of vibrations of the sprung mass compared to the N.O. version (compare index $J_{3,4}$ in case C4 with case C5). It follows that the development of the designed ECU should concern only the N.C. version;
- The ECU version developed so far is not able to provide power for the displacement sensors (linear magnetic encoders) used in the described tests.

Considering the above, further research will be focused on expanding the ECU with stored-energy management circuits and introducing linear accelerometers (MEMS), which are characterized by much lower power consumption, into the VRS instead of linear encoders. The possibility of using the output voltage signal of the harvester to reproduce the relative speed will also be tested, which will allow the elimination of one of the sensors. Other MR damper control algorithms will also be tested.

Author Contributions: Conceptualization, B.S.; design and simulation of the electrical control unit, A.K.; preparation of the experimental setup, Ł.J.; software implementation for the microcontroller, A.K. and Ł.J.; planning of experimental tests, B.S. and Ł.J.; carried out experiments and processed data, A.K. and Ł.J.; data validation and supervision, B.S. All the authors provided critical feedback and helped shape the research. All authors have read and agreed to the published version of the manuscript.

Funding: This work is supported by AGH University of Science and Technology under research program No. 16.16.130.942.

Conflicts of Interest: The authors declare no conflict of interest.

References

1. Wei, C.; Jing, X. A comprehensive review on vibration energy harvesting: Modelling and realization. *Renew. Sustain. Energy Rev.* **2017**, *74*, 1–18. [CrossRef]
2. Anton, S.R.; Sodano, H.A. A review of power harvesting using piezoelectric materials (2003–2006). *Smart Mater. Struct.* **2007**, *16*, R1. [CrossRef]
3. Safaei, M.; Sodano, H.A.; Anton, S.R. A review of energy harvesting using piezoelectric materials: State-of-the-art a decade later (2008–2018). *Smart Mater. Struct.* **2019**, *28*, 113001. [CrossRef]
4. Zou, A.; Liu, Z.; Han, X. A Low-Power High-Efficiency Adaptive Energy Harvesting Circuit for Broadband Piezoelectric Vibration Energy Harvester. *Actuators* **2021**, *10*, 327. [CrossRef]
5. Saha, C.R.; O'Donnell, T.; Wang, N.; McCloskey, P. Electromagnetic generator for harvesting energy from human motion. *Sens. Actuators A Phys.* **2008**, *147*, 248–253. [CrossRef]
6. Molina Arias, L.; Iwaniec, J.; Iwaniec, M. Modeling and Analysis of the Power Conditioning Circuit for an Electromagnetic Human Walking-Inducted Energy Harvester. *Energies* **2021**, *14*, 3367. [CrossRef]
7. Sapiński, B. Vibration Power Generator for a Linear MR Damper. *Smart Mater. Struct.* **2010**, *19*, 5012. [CrossRef]
8. Sapiński, B. An experimental electromagnetic induction device for a magnetorheological damper. *J. Theor. Appl. Mech.* **2008**, *46*, 933–947.
9. Tang, X.; Lin, T.; Zuo, L. Design and optimization of a tubular linear electromagnetic vibration energy harvester. *IEEE/ASME Trans. Mechatron.* **2014**, *19*, 615–622. [CrossRef]
10. Duong, M.T.; Chun, Y.D.; Hong, D.K. Design of a high-performance 16-slot 8-pole electromagnetic shock absorber using a novel permanent magnet structure. *Energies* **2018**, *11*, 3352. [CrossRef]
11. Ahamed, R.; Ferdaus, M.M.; Li, Y. Advancement in Energy Harvesting Magneto-Rheological Fluid Damper: A Review. *Korea-Aust. Rheol. J.* **2016**, *28*, 355–379. [CrossRef]
12. Sarker, M.R.; Saad, M.H.; Olazagoitia, J.L.; Vinolas, J. Review of Power Converter Impact of Electromagnetic Energy Harvesting Circuits and Devices for Autonomous Sensor Applications. *Electronics* **2021**, *10*, 1108. [CrossRef]
13. Sapiński, B. Experimental Study of a Self-Powered and Sensing MR-Damper-Based Vibration Control System. *Smart Mater. Struct.* **2011**, *20*, 5007. [CrossRef]

14. Zhu, S.; Shen, W.A.; Xu, Y.L. Linear electromagnetic devices for vibration damping and energy harvesting: Modeling and testing. *Eng. Struct.* **2012**, *34*, 198–212. [CrossRef]
15. Cai, Q.L.; Zhu, S. Enhancing the performance of electromagnetic damper cum energy harvester using microcontroller: Concept and experiment validation. *Mech. Syst. Signal Process.* **2019**, *134*, 106339. [CrossRef]
16. Shen, W.; Zhu, S.; Xu, Y. An experimental study on self-powered vibration control and monitoring system using electromagnetic TMD and wireless sensors. *Sens. Actuators A Phys.* **2012**, *180*, 166–176. [CrossRef]
17. Shen, W.; Zhu, S.; Zhu, H. Experimental study on using electromagnetic devices on bridge stay cables for simultaneous Energy harvesting and vibration damping. *Smart Mater. Struct.* **2016**, *25*, 065011. [CrossRef]
18. Takeya, K.; Sasaki, E.; Kobayashi, Y. Design and parametric study on energy harvesting from bridge vibration using tuned dual-mass damper systems. *J. Sound Vib.* **2016**, *361*, 50–65. [CrossRef]
19. Balato, M.; Costanzo, L.; Vitelli, M. Resonant electromagnetic vibration harvesters: Determination of the electric circuit parameters and simplified closed-form analysis for the identification of the optimal diode bridge rectifier DC load. *Int. J. Electr. Power Energy Syst.* **2017**, *84*, 111–123. [CrossRef]
20. Sapiński, B.; Węgrzynowski, M.; Nabielec, J. Magnetorheological damper–based positioning system with power generation. *J. Intell. Mater. Syst. Struct.* **2018**, *29*, 6. [CrossRef]
21. Sapiński, B.; Jastrzębski, Ł.; Kozieł, A. Ideal Rectifier Bridge Converting the Harvested Energy of Vibrations Into Electric Energy to Power an MR Damper. *Acta Mech. Autom.* **2020**, *14*, 198–205. [CrossRef]
22. Sapiński, B.; Orkisz, P.; Jastrzębski, Ł. Experimental Analysis of Power Flows in the Regenerative Vibration Reduction System with a Magnetorheological Damper. *Energies* **2021**, *14*, 848. [CrossRef]
23. Jastrzębski, Ł.; Sapiński, B. Magnetorheological Self-Powered Vibration Reduction System with Current Cut-Off: Experimental Investigation. *Acta Mech. Autom.* **2018**, *12*, 96–100. [CrossRef]
24. STMicroelectronics, Technical Documentation. Available online: http://www.st.com/ (accessed on 9 December 2021).
25. Texas Instruments, Technical Documentation. Available online: https://www.ti.com/ (accessed on 9 December 2021).
26. Analog Devices. Available online: https://www.analog.com/en/index.html (accessed on 9 December 2021).
27. Nexperia, Technical Documentation. Available online: https://www.nexperia.com (accessed on 9 December 2021).
28. Fluke, Technical Documentation. Available online: https://www.fluke.com (accessed on 9 December 2021).
29. MR damper, RD-8040-1, Technical Documentation. Available online: https://www.lord.com (accessed on 9 December 2021).
30. Lika, Technical Documentation. Available online: https://www.lika.it/eng (accessed on 9 December 2021).
31. Choi, S.-B.; Li, W.; Yu, M.; Du, H.; Fu, J.; Do, P.-X. State of the art of control schemes for smart featuring magneto-rheological materials. *Smart Mater. Struct.* **2016**, *25*, 043001. [CrossRef]
32. Karnopp, D.; Crosby, M.; Harwood, R. Vibration Control Using Semi-Active Force Generators. *ASME J. Eng. Ind.* **1974**, *96*, 619–626. [CrossRef]
33. Savaresi, S.M.; Poussot-Vassal, C.; Spelta, C.; Sename, O.; Dugard, L. *Semi-Active Suspension Control Design for Vehicles*; Butterworth-Heinemann/Elsevier: Oxford, UK, 2010.
34. Smoter, A.; Sibielak, M. Experimental and numerical investigation of the active double wishbone suspension system. In Proceedings of the 20th International Carpathian Control Conference ICCC, Krakow-Wieliczka, Poland, 26–29 May 2019.